Submitted to Mater. Sci. Eng. A: August 2014.
Revision I: October 2014

Grain refinement and high strain rate superplasticity in alumunium 2024 alloy Processed by high-pressure torsion

Ali Alhamidi[1, 2], Zenji Horita[1, 2]

[1]Department of Materials Science and Engineering, Faculty of Engineering, Kyushu University, Fukuoka 819-0395, Japan
[2]WPI, International Institute for Carbon-Neutral Energy Research (WPI-I2CNER), Kyushu University, Fukuoka 819-0395, Japan

An Al-2024 alloy was processed by high-pressure torsion (HPT) to produce an ultrafine-grained structure with a grain size of ~240 nm. A maximum elongation of ~750% was attained with an initial strain rate of 1×10^{-2} s^{-1} at 673 K, demonstrating the advent of high strain rate superplasticity through grain refinement by the HPT processing. Evaluation of the strain-rate sensitivity and the activation energy for the deformation confirmed that grain boundary sliding through grain boundary diffusion is the rate-controlling process for the superplastic deformation of the HPT-processed Al-2024 alloy.

Corresponding author: Ali Alhamidi
TEL/FAX: +81-92-802-2992; e-mail: ali@zaiko6.zaiko.kyushu-u.ac.jp.

1. Introduction

Superplastic materials have been widely used in many applications in automotive and aerospace industries because they offered several benefits such as reduced weight for high fuel efficiency, improved structural performance, increased metal formability and low-cost tooling [1]. As well known, the major problem in utilizing the superplasticity is that the strain rate is slow as in the range of ~10^{-4}-10^{-3} s^{-1} [2]. This becomes a drawback in applying the superplasticity for manufacturing industries. In order to overcome such a drawback, much effort has been devoted to develop high-strain-rate superplasticity (HSRS), typically in the strain rate range > 10^{-2} s^{-1} or close to the commercial hot working rates of ~10^{-1} to 10^{2} s^{-1} [3], in several alloys and composites [2-11].

Aluminum 2024 alloys has been reported to have high strength and good damage tolerance due to precipitation of Al_2CuMg particles [12,13]. Some investigations concerning HSRS of an Al-2024 alloy were reported by Lee *et al*. [14] with a maximum elongation of 500% at a temperature of 673 K after processing by equal-channel angular pressing (ECAP), by Dobatkin *et al*. [15] with a maximum elongation of 570% at a temperature of 673 K after processing by high-pressure torsion (HPT), and by Charit *et al*. [8] with a maximum elongation of 525% at 703 K after processing by friction stir processing (FSP). The highest elongation of 1830% was attained after thermo-mechanical treatment (TMT) by Zheng and Baoliang [16] but the strain rate below 1.3 × 10^{-3} s^{-1} is rather slow and the testing temperature of 773 K is high.

It is well established that grain refinement is of prime importance for the attainment of HSRS [3]. Processing through SPD such as ECAP and HPT are a practical

means for the reduction in grain size to the submicrometer and/or nanometer scale. In particular, HPT is promising for the grain refinement as it is capable of more refining the grain size than any other SPD processes [17] and it is applicable to hard and brittle materials such as intermetallics [18,19] and ceramics [20] because of the straining under high pressure. However, micostructural development may be inhomogeneous across the diameter of the disk for HPT processing, and thus, as reported by Dobatkin *et al*. [15], the grain refinement is less achieved around the center of the disk but better at the outer area of the disk. Accordingly, superplasticity appeared at the latter areas. Based on such a report, we carry out a comprehensive experiment in this study to examine strain rate dependence (*ie*., strain rate sensitivity) and temperature dependence (*ie*., activation energy), and therefore to understand the mechanism involved in the superplasticity of the Al-2024 alloy.

2. Experimental procedures

The experiment was undertaken using a commercially availablle AA2024-T4 alloy with a rod-shape billet having 10mm diameter with the composition as listed in Tabel 1. The rod was sliced by using an electrical-discharge machine (EDM) into discs having 1mm thickness. The discs were subjected to solution treatment (hereafter, called S.T.) for 12 hours at a temperature of 793 K and quenched into ice-water prior to HPT processing. Each of the discs was subsequently processed between two anvils and strained by concurrent rotation of the two anvils with respect to each other for either N = 0.75, 1 or 5 revolutions under a pressure of 6 GPa at room temperature (R.T.) with an HPT machine described earlier [17,35].

The HPT-processed discs were first polished to a mirror-like surface and Vickers

microhardness was measured with an applied load of 200 g for 15 s along the radii at twelve different radial directions. Furthermore, for preparation of tensile specimens, the S.T. disc and the HPT-processed discs were polished using abbrasive papers to total thicknesses of 0.5 - 0.7 mm and tensile specimens having gauge lengths and gauge widths of 1.5 mm and 3.5 mm, respectively, were extracted from the polished discs at the off-centered positions using the EDM. Each of the tensile specimens was mounted horizontally in grips within the furnace. Tensile tests were carried out at 573, 623, 673 and 723 K with an initial strain rate of 2×10^{-2} s^{-1} for the S.T. sample and with an initial strain rate in the range from 2×10^{-3} to 2×10^{-2} s^{-1} for the HPT-processed sample.

In order to measure grain size before the HPT processing, the S.T. sample was cut and polished to a mirror-like surface using abrasive papers followed by buffing with alumina-containing cloth. The sample was etched in a mixture of 50 ml HNO_3 and 50 ml distillated-water. Figure 1 shows a typical low magnification optical micrograp taken on such samples. It was found that the average grain size of ~33 μm.

Microstructure observations of the samples processed by HPT and post-HPT annealing were conducted using transmission electron microscopy (TEM). Discs with 3mm diameter were punched out at 3mm away from the disc center, ground to a thickness of ~0.15 mm using abrasive papers. The discs were then thinned using a twin-jet electrochemical polisher in a solution of 80% CH_3OH and 20% HNO_3 at 263 K under 10 V. Selected area electron diffraction (SAED) analysis was carried out using an apperture size of ~1.6 μm. TEM was conducted at 200 kV using a Hitachi-8100. The surface morphology was analysed by using a HITACHI S-4300SE Scanning Electron Microscope (SEM) operating at 20 kV on the sample after tensile testing. Presence of second-phases were analyzed by X-ray diffraction (XRD) analysis using the Cu Kα

radiation in a scanning step of 0.02° and a scanning speed of 0.5°/min and determined using the software of International Center for Diffraction Data, ICDD 2000, JCPDS v.2.1.

3. Results

Figure 2 plots Vickers microhardness against (a) the distance from the disc center and (b) the shear strain after processing by HPT for N = 0.75, 1 and 5 revolutions at room temperature. The hardness level for the solution-treated sample is also included in Fig.2(a) and (b). The shear strain, γ, was calculated using Eq. (1) [17].

$$\gamma = \frac{2\pi rN}{h} \qquad (1)$$

where r is the distance from the disc center, N is the number of revolutions and h is the thickness of disc. It is apparent that the hardness increases with an increase in γ at an early stage of straining and saturates to a steady-state level of ~250 Hv at γ>~20, where the hardness remains unchanged with straining.

Figure 3 shows a TEM bright-field image (left), dark-field image (right) and SAED pattern (center) for the sample processed by HPT for N = 5 under 6 GPa at room temperature, of which condition well corresponds to the steady state. The dark-field image was taken using the diffracted beam indicated by an arrow in the SAED pattern. This observation reveals that the microstucture consists of grains having an average grain size of ~240 nm. Many spots are scattered around circles in the SAED pattern in Fig.3 and this confirms the presence of ultrafine grains with high angles of misorientations.

Figure 4 shows TEM bright-field images (left), dark-field images (center) and the

corresponding SAED patterns for HPT-processed samples after annealing at temperatures of (a) 573, (b) 623 and (c) 723 K for 1h. The dark-field images were taken using the diffracted beam indicated by arrows in the SAED patterns. It is apparent that grain coarsening occurred to the sizes of ~500, ~1000 and ~1600 nm following the anealing, respectively. Close analysis of the SAED pattern confirms the presence of second-phase particles within the Al matrixs as indicated by arrows in the bright-field images. It should be noted that particle **A** in Fig.4(b) corresponds to an Al_3Fe precipitate and this is confirmed by the SAED pattern obtained from a region including partcile **A** as shown in Fig. 5.

Figure 6 shows XRD profiles for the sample processed by HPT and subsequently annealed at 623 K for 1 h. Inspection reveals that several peaks corresponding to second-phases particles such as Al_3Fe, Al_6Mn, Al_2Cu and Al_2CuMg are visible other than the peaks from the Al matrix. It is considered that such second-phase particles are responsible for reducing the grain growth during the annealing.

Figure 7 shows the nominal stress–strain curves of the S.T. samples tested in tension in the temperature range from room temperature (R.T) to 723 K with an initial strain rate of 1×10^{-2} s^{-1}. The highest ultimate tensile strength was achieved at R.T, then the flow stress decreased and the ductility increased with an increase in testing temperature. However, the total elongation is insufficient for superplasticity.

Figure 8 shows the nominal stress-strain curves of samples deformed in tension at temperatures of (a) 573 K, (b) 623 K, (c) 673 K and (d) 723 K with strain rates in the range from 1×10^{-3} s^{-1} to 2×10^{-2} s^{-1} after processing by HPT for $N = 5$. It is apparent that the maximum flow stress decreases with decreasing the strain rate at all testing temperatures and with increasing the testing temperature at a given strain rate. It is also

apparent that superplasticity with the total elongation more than 400% was well achieved at testing temperatures of 573 K and 623 K with all strain rates covered in this study including the strain rates higher than 1×10^{-2} s^{-1}. The highest elongation of ~750% was attained at the temperature of 673 K with the initial strain rate of 1×10^{-2} s^{-1}.

The appearance of the tensile specimens after tensile testing is shown in Fig.9 at the four different temperatures with the strain rate range from 1×10^{-3} to 2×10^{-2} s^{-1} including undeformed samples. It is confirmed that the deformation occurs uniformly without necking along the gauge length as the total elongation is increased.

Figure 10 shows a comparison of the maximum elongation obtained in this study with published results [8,14-16]. It is demonstrated that the HSRS with 1×10^{-2} s^{-1} is achieved at lower temperatures in this study and the total elongation is higher than any other reported values at the lower temperatures. The smaller grain size of ~240 nm produced by the HPT processing should be responsible for the higher elongation because the superplasticity obtained in this study is controlled by grain boundary sliding as discussed below. It is noted that the grain sizes reported in the other studies are 300-500 nm [8], 3900 nm [14], 300 nm [15] and 2500 nm [16], all of which are larger than ~240 nm of this study. The total elongation to failure increases with temperature, reaches a peak at 673 K and decreases with the further increase in temperature. The former increase in the total elongation with temperature is because the grain boundary sliding is more activated with an effect of temperature but at higher temperatures as above 673 K, grain growth occurs so that the contribution of the grain boundary sliding to the total strain decreases because of a decrease in the grain boundary fraction.

4. Discussion

In order to understand the mechanism controlling the superplastic deformation in the Al-2024 alloy, the analysis using the following equation may be useful [21,23].

$\dot{\varepsilon} = A\left(\frac{b}{d}\right)^{p}\left(\frac{\sigma}{G}\right)^{n}\exp\left(-\frac{Q}{RT}\right)$	(2)

where A is a constant, σ is the flow stress, G is the shear modulus, n is the stress exponent and is equivalent to the reciprocal of the strain rate sensitivity m as $(m = 1/n)$, b is the Burgers vector, d is the grain size, p is the grain-size exponent, Q is the activation energy for deformation, R is the gas constant, and T is the testing temperature. It is well established that the superplastic deformation is a diffusion-controlled process and is facilitated by grain boundary sliding (GBS) [22-37], where the value of n normally takes 2 (ie., m=0.5). Now, the maximum flow stress is plotted against the initial strain rate in Fig. 11 in a double logarithmic relationship. It is found that a linear relationship reasonably holds at each testing temperature. Because the slope in Fig.11 corresponds to m and it is in the range of $m \approx 0.33$-0.42, it turns out that the results are well consistent with the strain rate sensitivity reported for superplasticity controlled by GBS [22-38]. Although it is difficult to evaluate the grain size dependence, p, because grain growth occurs during tensile testing including heating before the tensile testing and cooling after the tensile testing as shown in Fig.4, it is possible to evaluate the temperature dependence through the activation energy, Q. In this study, the value of Q was evaluated such that the strain rate taken at the flow stress of 10 MPa is plotted against the reciprocal of the testing temperature. As shown in Fig. 12, a good linear relationship holds between the two parameters and thus the slope gives rise to $Q \approx 72$ kJ/mol. This

value is in good agreement with the activation energy for grain boundary diffusion in pure Al ≈ 72 kJ/mol [39]. It is thus concluded that the superplastic deformation of the present alloy is controlled by grain boundary sliding through grain boundary diffusion.

The occurrence of the grain boundary sliding should be demonstrated more directly by the SEM image as shown in Fig. 13 for the specimen deformed at 673 K with a strain rate of 1×10^{-2} s^{-1}. The observation was undertaken at positions of **A**, **B** and **C**, after deformation to ~750% and the representative micrographs are shown in (a), (b) and (c), respectively. Most of the grains retain equaxied configurations with grain size ~4 μm, as shown in Fig. 13(a). However, the grain shape changed to elongated configurations with grains of 12 μm and 18 μm in longer axis in Fig. 13(b) and Fig.13 (c), respectively. Nevertheless, such elongations of the grain are insufficient to account for the total elongation of ~750%. It is suggested that grain boundary sliding occurs by mutual change in positions and to some degree in shape of grains in the tensile direction (TD).

The annealing of the HPT-processed samples led to grain growth from the initial size of 240 nm after HPT processing to the sizes of ~500, ~1000 and ~1600 nm after annealing at 573, 673 and 723 K for 1 h, respectively. The grain growth occurred irrespective of the annealing temperatures but it is still within the range to generate superplastic flow. The inhibition of the significant grain growth should be due to the presence of additional impurity elements such as Mn and Fe which led to the formation of second-phase particles as Al_6Mn, Al_2Cu, Al_2CuMg and Al_3Fe as detected in the XRD profiles of Fig. 6 and as marked **A** in Fig. 4 and Fig. 5. Similar observation concerning the stability at an elevated temperature in an Al-2024 alloy was reported by Vafaei *et al* [13]. Their investigation using Energy Dispersive Spectroscopy (EDS) indicated the

presence of second phase particles of $Al_{20}Cu_2Mn_3$, $Al_{12}Mg_2Cr$ and $ZrAl_3$ which retarded the occurrence static recrystallization and grain growth in the alloy.

5. Summary and Conclusion

1. Grain refinement to ~240 nm with high-angle misorientation was achieved through high-pressure torsion.
2. The superplastic elongation of ~750% at 673 K with $\dot{\varepsilon} = 1 \times 10^{-2}$ $s^{-1}$was well higher than reported in earlier papers.
3. The strain rate sensitivity of $m \approx 0.4$ was obtained, which is close to the value suggested for superplastic deformation through grain boundary sliding.
4. The activation energy, Q, for the deformation was ~72 kJ/mol which is comparable to the activation energy for grain boundary diffusion in Al (72.2 kJ/mole). The mechanism of the superplasticity attained in the Al-2024 alloy is the grain boundary sliding controlled by grain boundary diffusion..
5. Presence of Cu, Mn and Fe in the Al-2024 alloy led to the formation of second phase particles acting as inhibitors for grain growth and contributing to the stability of the fine-grained structure at elevated temperatures.

Acknowledgements

One of the authors (AA) would like to thank Indonesian Government for a PhD scholarship through the Directorate of Higher Education Program (DGHE). This work was supported in part by Japan Science and Technology Agency (JST) under Collaborative Research Based on Industrial Demand “Heterogeneous Structure Control: Towards Innovative Development of Metallic Structural Materials”, in part by the Light

Metals Educational Foundation of Japan and in part by a Grant-in-Aid for Scientific Research from the MEXT, Japan, in Innovative Areas "Bulk Nanostructured Metals" 22102004.

Tabel Captions

Tabel 1. Composition of Al-2024 alloy. Unit in mass%

Figure Captions

Figure 1. Optical micrograph of Al-2024 alloy after solution treatment.

Figure 2. Vickers microhardness plotted against (a) distance from disc center and (b) shear strain for samples processed by HPT through N = 0.75, 1 and 5 revolutions, including sample after solution treatment.

Figure 3. TEM bright-field images (left), dark-field image (right) and corresponding SAED patterns (center) for samples processed by HPT for N = 5 at R.T. Dark-field image was taken by diffracted beam indicated by arrow in SAED pattern.

Figure 4. TEM bright-field images (left), dark field images (center) and corresponding SAED patterns (right) after HPT processing for N = 5 and subsequent annealing at (a) 573 K, (b) 623 K and (c) 723 K for 1 h. Dark-field images were taken by diffracted beams indicated by arrows in SAED patterns. Arrows in bright-field images indicate particles.

Figure 5. TEM bright-field image (left) and SAED pattern (right) of Al_3Fe correspond to particle **A** in Fig. 4(b).

Figure 6. XRD profiles after HPT processing and subsequent annealing for 1 h at 623 K.

Figure 7. Nominal stress versus nominal strain for solution-treated (ST) samples and tensile tested at RT, 573 K, 623 K, 673 K, and 723 K with strain rate of 1×10^{-2} s^{-1}.

Figure 8. Nominal stress versus nominal strain for samples processed by HPT through N = 5 revolutions and tensile tested at (a) 573 K, (b) 623 K, (c) 673 K, and (d) 723 K.

Figure 9. Appearance of tensile specimens after deformation to failure including undeformed specimens for testing temperatures of 573, 623, 673 and 723 K.

Figure 10. Maximum elongation to failure with testing temperature for HPT-processed samples including published data with use of FSP [8], ECAP [14], HPT [15] and TMT [16].

Figure 11. Maximum stress plotted against initial strain rate with strain rate sensitivity, m.

Figure 12. Plots of strain rates taken at stress level of 10 MPa in Fig.11 against reciprocal temperature.

Figure 13. Scanning electron microscope (SEM) for sample processed by HPT through $N = 5$ revolutions followed by tensile testing at temperature of 673 K with initial strain rate of 1×10^{-2} s^{-1} for maximum elongation of ~750%. (a), (b) and (c) correspond to positions **A**, **B** and **C**, respectively, for observation. SEM images of tensile specimen deformed to maximum elongation of ~750% at 673 K with initial strain rate of 1×10^{-2} s^{-1}. (a), (b) and (c) correspond to positions **A**, **B** and **C** on deformed specimen, respectively.

References

[1] A.J. Barnes, J. Mater. Eng. Perform. 16 (2007) 440-454.

[2] C.F. Yang, J.H. Pan, M.C. Chuang, J. Mater. Sci. 43 (2008) 6260-6266.

[3] K. Higashi, Met. Mater. Int. 4 (1998) 498-502.

[4] V. N. Perevezentsev, M. Yu. Shcherban, M. Yu. Murashkin, R. Z. Valiev, Tech. Phys. Lett. 33 (2007) 648-650.

[5] R.S. Mishra, JOM 53 (2001) 23-26.

[6] T.D. Wang, J.C. Huang, Mater. Trans. JIM 42 (2001) 1781-1789.

[7] T.R. Bieler, R.S. Mishra , A.K. Mukherjee, JOM 48 (1996) 52-56.

[8] I. Charit, R.S. Mishra, Mater. Sci. Eng. A 359 (2003) 290-296.

[9] T.G. Nieh, L.M. Hsiung, J. Wadsworth, R. Kaibyshev, Acta Mater. 46 (1998) 2789-2800.

[10] Z. Horita, M. Furukawa, M. Nemoto, A.J. Barnes, T.G. Langdon, Acta Mater. 48 (2000) 3633-3640.

[11] V.V. Astanin, O.A. Kaibyshev, L.A. Imayeva, A.A. Sirenko J. Mater. Eng. Perform. 6 (1997) 461- 468.

[12] J.C. Malas, S. Venugopal, T. Seshacharyulu, Mater. Sci. Eng. A 368 (2004) 41-47.

[13] R. Vafaei, M.R. Toroghinejad, R. Pippan, Mater.Sci. Eng. A 536 (2012) 73-81.

[14] S. Lee, M. Furukawa, Z. Horita, T.G. Langdon, Mater. Sci. Eng. A 342 (2003) 294-301.

[15] S.V. Dobatkin, E.N. Bastarache, G. Sakai, T. Fujita, Z. Horita, T.G. Langdon, Mater. Sci. Eng. A 408 (2005) 141-146.

[16] W. Zheng, Z. Baoliang, J. Mater. Sci. Lett. 13 (1994) 1806-1808.

[17] A.P. Zhilyaev, T.G. Langdon, Progress in Mater. Sci. 53 (2008) 893-979.

[18] K. Edalati, S. Toh, M. Watanabe, Z. Horita, Scripta Mater. 66 (2012) 386-389.

[19] A. Alhamidi, K. Edalati, H. Iwaoka, Z. Horita, Philos. Mag. 94 (2014) 876-887.

[20] K. Edalati, S. Toh, Y. Ikoma, Z. Horita, Scripta Mater. 65 (2011) 974-977.

[21] O. D. Sherby, J. Wadsworth, Progress in Mater. Sci. 33 (1989) 169-221.

[22] T.G. Langdon, J. Mater. Sci. 44 (2009) 5998-6010.

[23] F.A. Mohamed, Mater 4 (2011)1194-1223.

[24] M. Kawasaki,T.G. Langdon , J. Mater. Sci. 42 (2007) 1782-1796.

[25] G. Sakai, Z. Horita, T.G. Langdon, Mater. Sci. Eng. A 393 (2005) 344-351.

[26] S. Katsas, R. Dashwood, R. Grimes, M. Jackson, G. Todd, H. Henein, Mater. Sci. Eng. A 444 (2007) 291-297.

[27] K. Neishi, Z. Horita, T.G. Langdon, Mater. Sci. Eng. A 352 (2003) 129-135.

[28] P. Kumar, C. Xu, T.G. Langdon, Mater. Sci. Eng. A 410–411 (2005) 447- 450.

[29] P. Malek, K. Turba, M. Cieslar, I. Drbohlav, T. Kruml, Mater. Sci. Eng. A 462 (2007) 95-99.

[30] R.B. Figueiredo, M. Kawasaki, C. Xu, T.G. Langdon, Mater. Sci. Eng. A 493 (2008) 104-110.

[31] R.B. Figueiredo, T.G. Langdon, Scripta Mater. 61 (2009) 84-87.

[32] S. Komura, Z. Horita, M. Furukawa, M. Nemoto, T.G. Langdon, Metall. Mater. Trans. A 32 A (2001) 707-716.

[33] Y. Miyahara, K. Matsubara, Z. Horita, T.G. Langdon, Metall. Mater. Trans. A 36A (2005) 1705-1711.

[34] C. Xu, S.V. Dobatkin, Z. Horita, T.G. Langdon, Mater. Sci. Eng. A 500 (2009) 170-175.

[35] Z. Horita, T.G. Langdon, Scripta Mater. 58 (2008) 1029-1032.

[36] J.M. Garcia-Infanta, A.P. Zhilyaev, A. Sharafutdinov, O.A. Ruano, F. Carreno, J. Alloys Compd. 473 (2009) 163-166.

[37] F.C. Liu, Z.Y. Ma, Scripta Mater. 59 (2008) 882-885.

[38] S. Lee, A. Utsunomiya, H. Akamatsu, K. Neishi, M. Furukawa, Z. Horita, T.G. Langdon, Acta Mater. 50 (2002) 553-564.

[39] H. Mehrer, Numerical Data and Functional Relationship in Science and Technology, Diffusion in Solid Metals and Alloys. Springer, vol. 26, Berlin(1990).

Tabel. 1

Cr	Cu	Fe	Mg	Mn	Si	Ti	Zn	Al
0.04	4.4	0.24	1.5	0.62	0.5	0.15	0.25	Balance

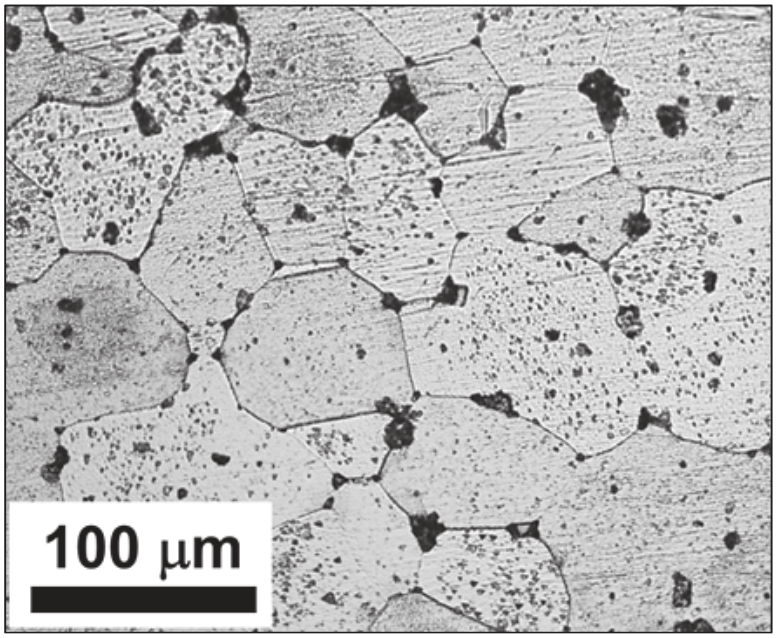

Figure 1

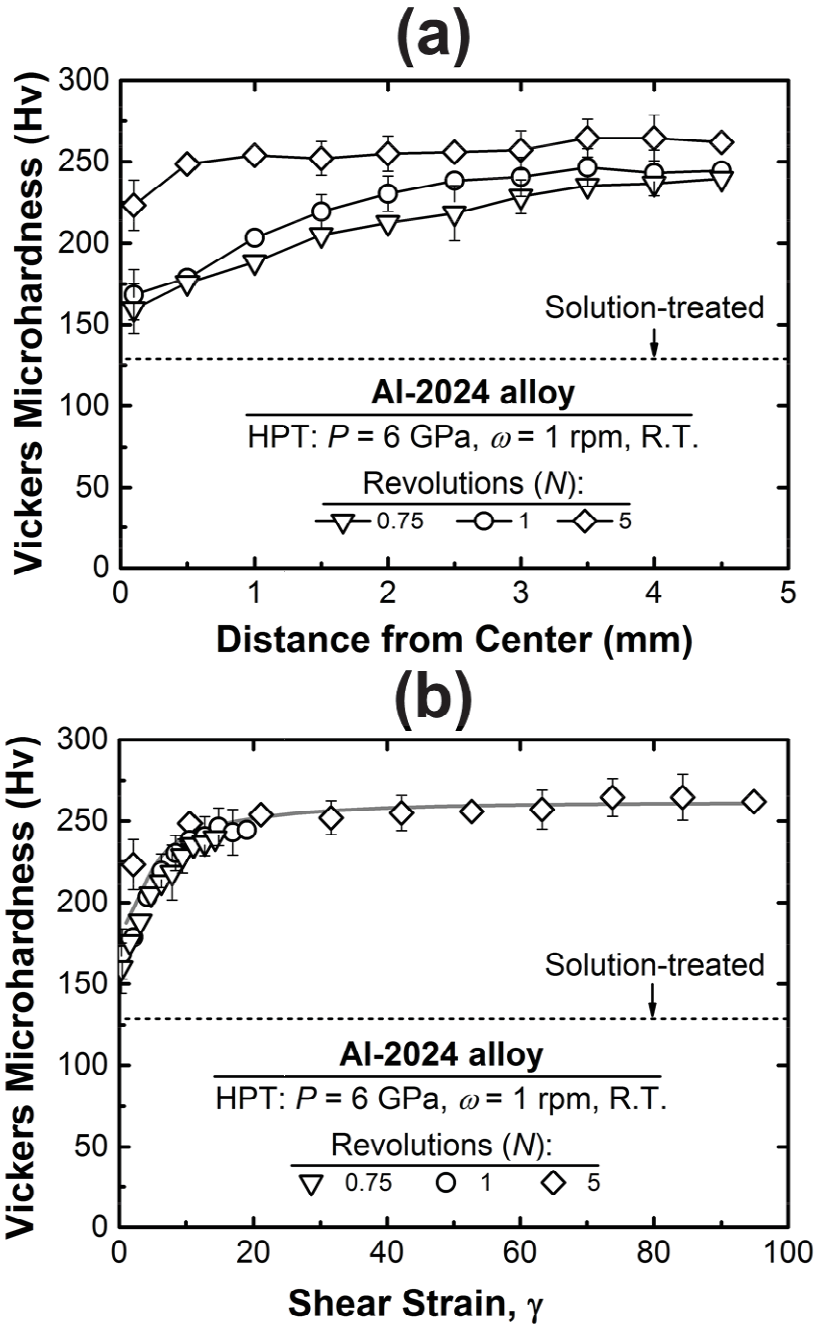
(a)
Vickers Microhardness (Hv)
Distance from Center (mm)
Solution-treated
Al-2024 alloy
HPT: P = 6 GPa, ω = 1 rpm, R.T.
Revolutions (N):
0.75
1
5
(b)
Vickers Microhardness (Hv)
Shear Strain, γ
Solution-treated
Al-2024 alloy
HPT: P = 6 GPa, ω = 1 rpm, R.T.
Revolutions (N):
0.75
1
5

Figure 2

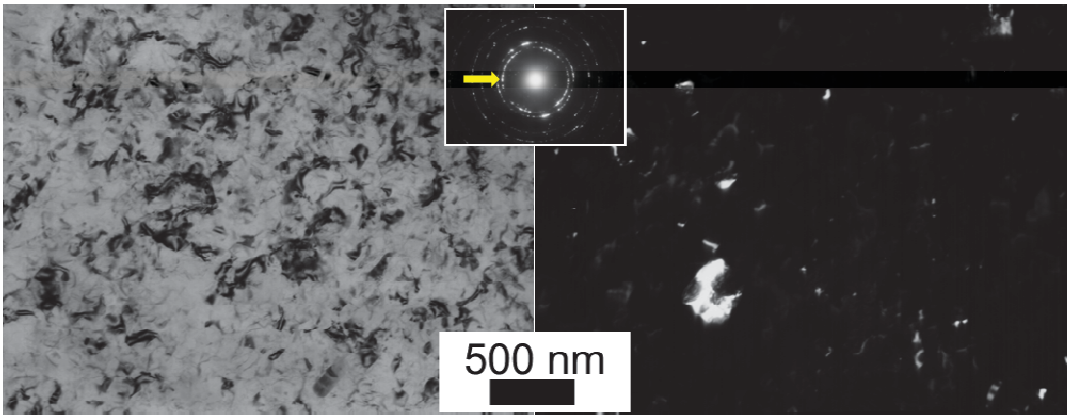

Figure 3

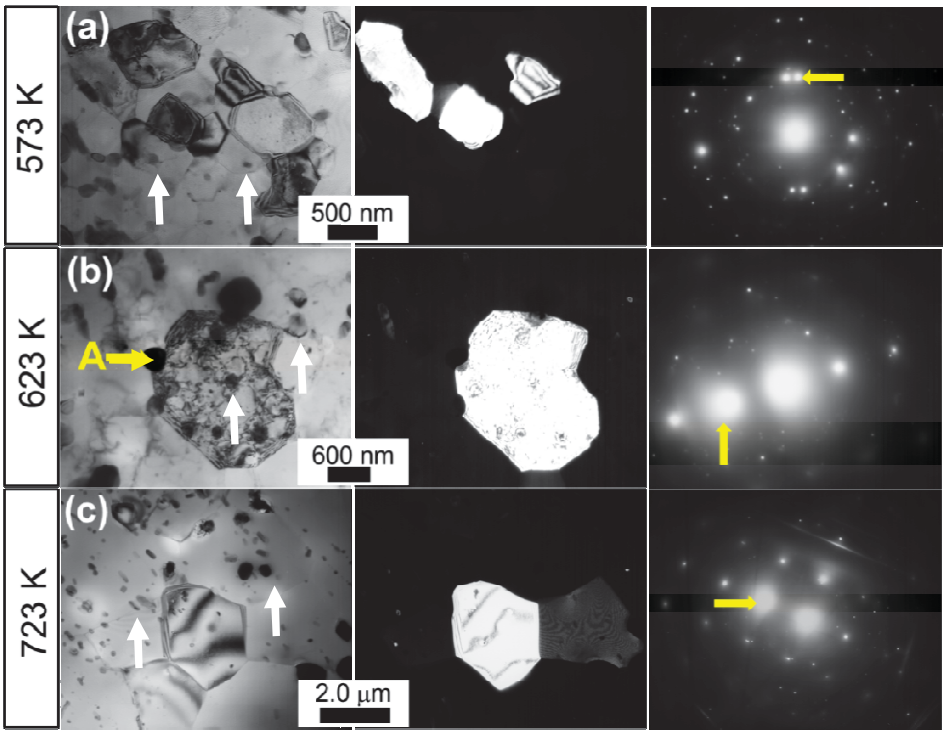

Figure 4

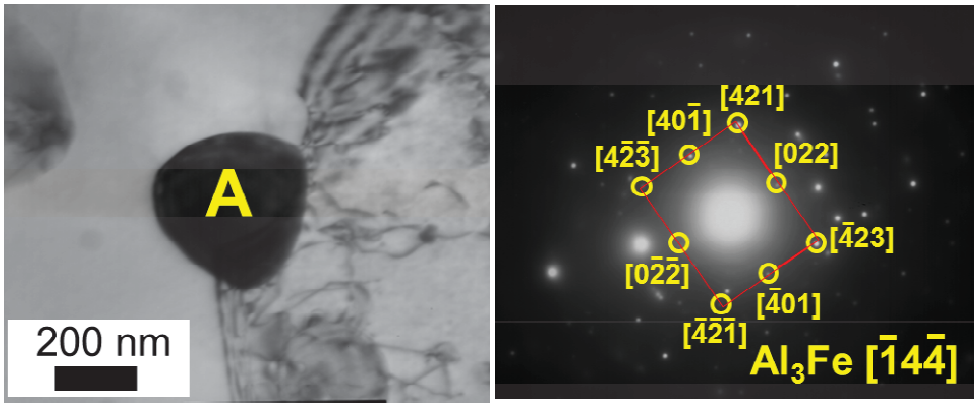
A
200 nm
[421]
[40$\bar{1}$]
[4$\bar{2}\bar{3}$]
[022]
[$\bar{4}$23]
[0$\bar{2}\bar{2}$]
[$\bar{4}$01]
[$\bar{4}\bar{2}\bar{1}$]
Al_3Fe [$\bar{1}4\bar{4}$]

Figure 5

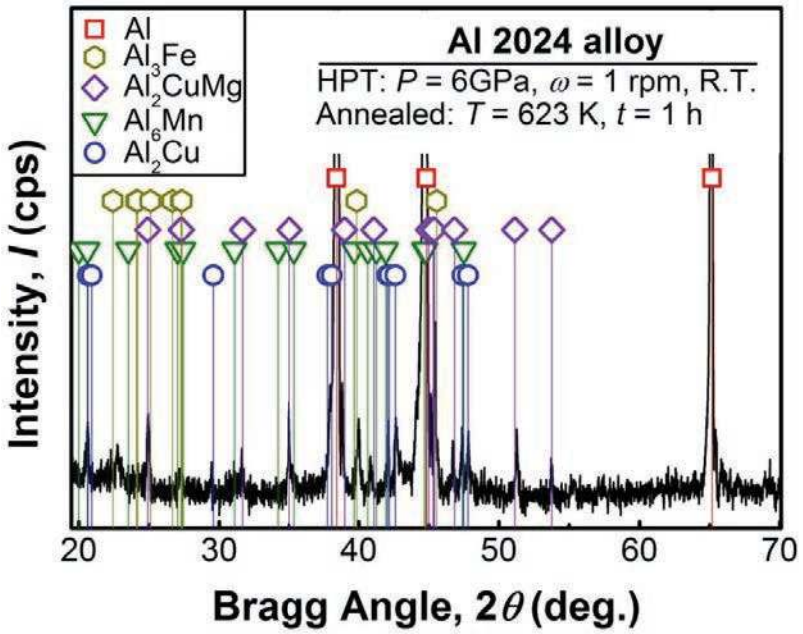
Al
Al3Fe
Al2CuMg
Al6Mn
Al2Cu
Al 2024 alloy
HPT: P = 6GPa, ω = 1 rpm, R.T.
Annealed: T = 623 K, t = 1 h
Intensity, I (cps)
20
30
40
50
60
70
Bragg Angle, 2θ (deg.)

Figure 6

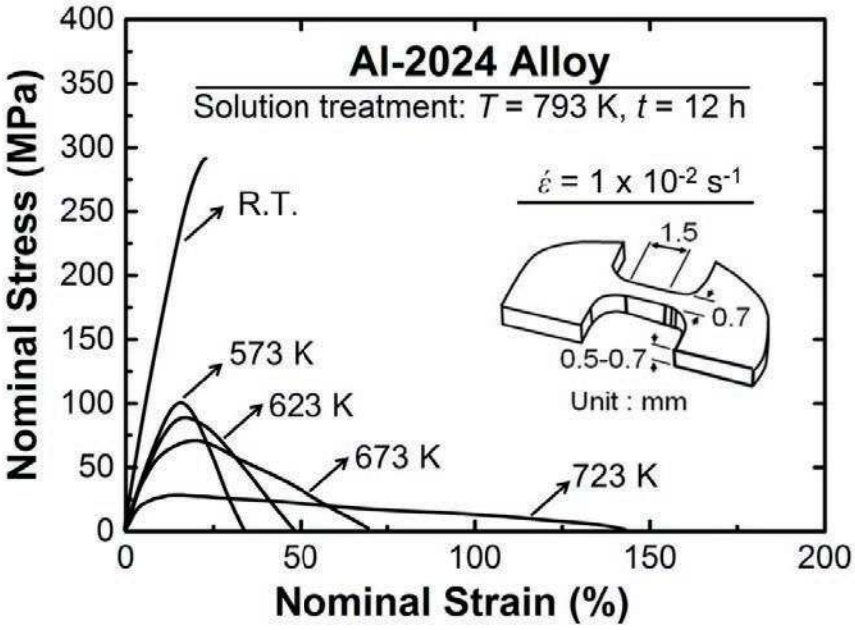
Al-2024 Alloy
Solution treatment: T = 793 K, t = 12 h
ε̇ = 1 x 10-2 s-1
R.T.
573 K
623 K
673 K
723 K
1.5
0.7
0.5-0.7
Unit : mm
Nominal Stress (MPa)
Nominal Strain (%)
0
50
100
150
200
250
300
350
400

Figure 7

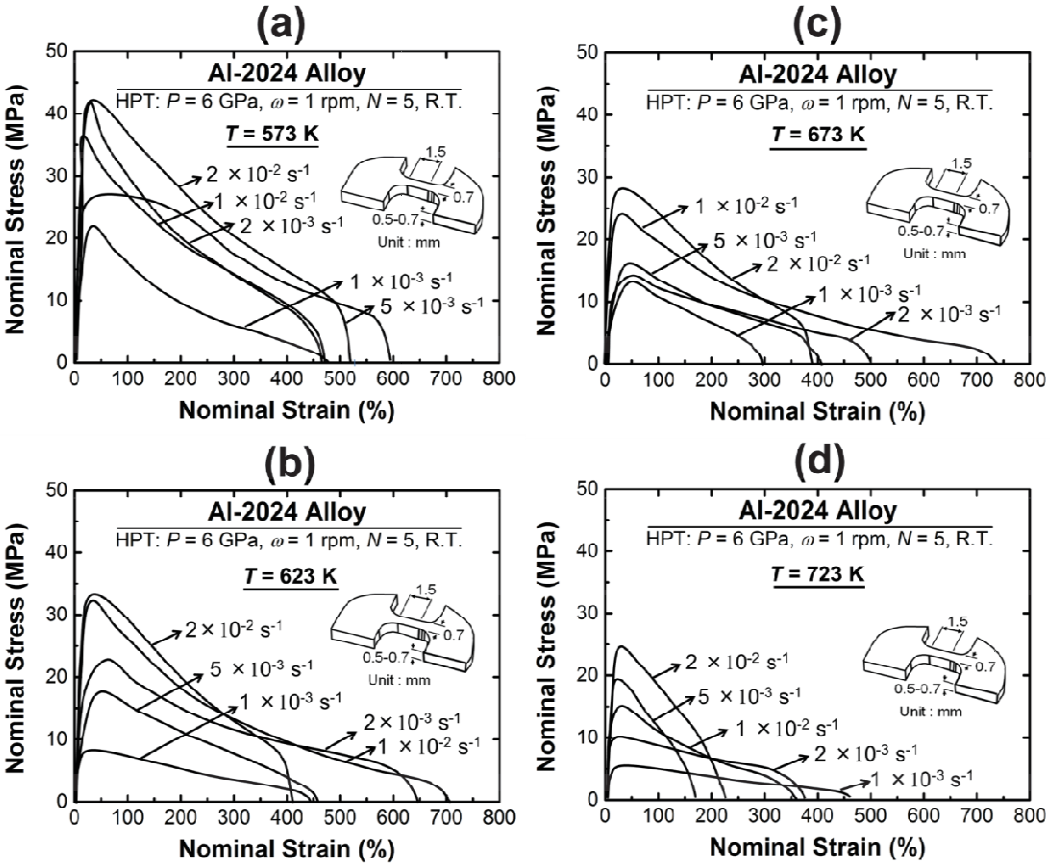
(a)
Al-2024 Alloy
HPT: P = 6 GPa, ω = 1 rpm, N = 5, R.T.
T = 573 K
2 × 10-2 s-1
1 × 10-2 s-1
2 × 10-3 s-1
1 × 10-3 s-1
5 × 10-3 s-1
Unit : mm
Nominal Stress (MPa)
Nominal Strain (%)
(c)
Al-2024 Alloy
HPT: P = 6 GPa, ω = 1 rpm, N = 5, R.T.
T = 673 K
1 × 10-2 s-1
5 × 10-3 s-1
2 × 10-2 s-1
1 × 10-3 s-1
2 × 10-3 s-1
Unit : mm
Nominal Stress (MPa)
Nominal Strain (%)
(b)
Al-2024 Alloy
HPT: P = 6 GPa, ω = 1 rpm, N = 5, R.T.
T = 623 K
2 × 10-2 s-1
5 × 10-3 s-1
1 × 10-3 s-1
2 × 10-3 s-1
1 × 10-2 s-1
Unit : mm
Nominal Stress (MPa)
Nominal Strain (%)
(d)
Al-2024 Alloy
HPT: P = 6 GPa, ω = 1 rpm, N = 5, R.T.
T = 723 K
2 × 10-2 s-1
5 × 10-3 s-1
1 × 10-2 s-1
2 × 10-3 s-1
1 × 10-3 s-1
Unit : mm
Nominal Stress (MPa)
Nominal Strain (%)

Figure 8

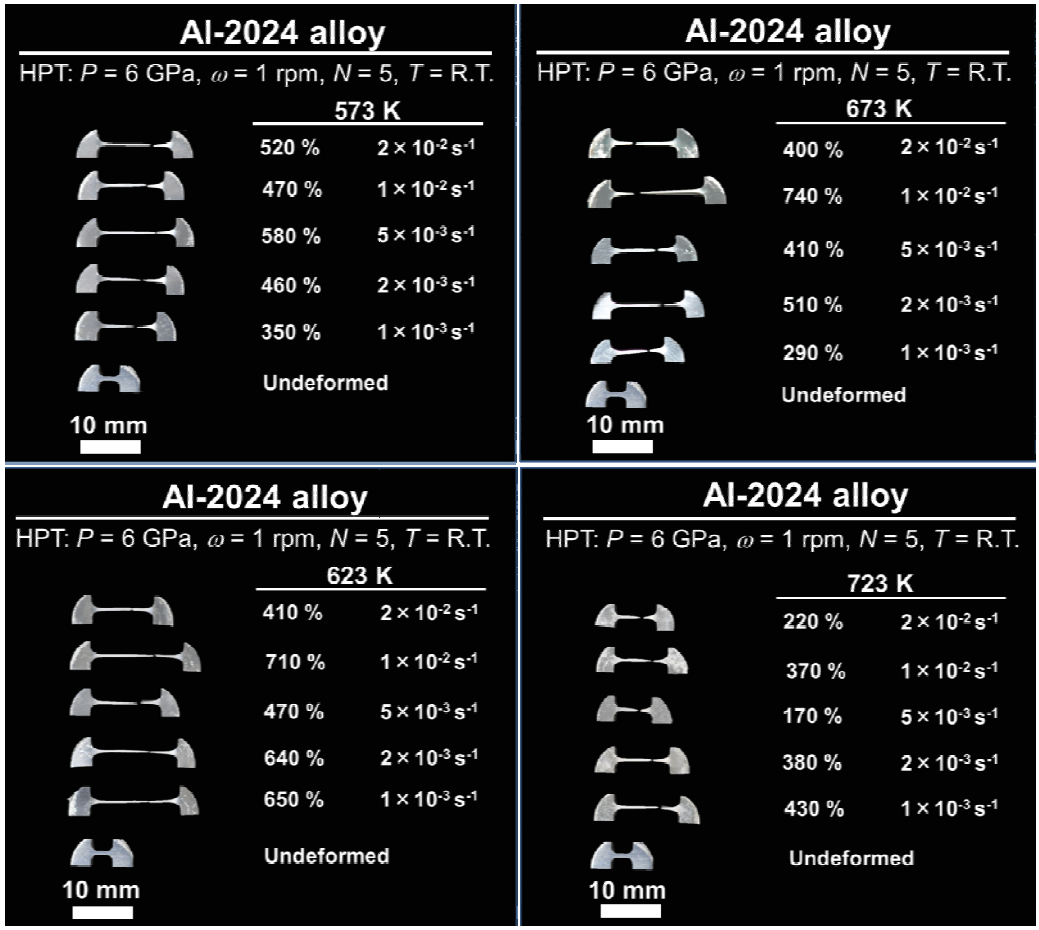
Al-2024 alloy
HPT: P = 6 GPa, ω = 1 rpm, N = 5, T = R.T.
573 K
520 % 2 × 10-2 s-1
470 % 1 × 10-2 s-1
580 % 5 × 10-3 s-1
460 % 2 × 10-3 s-1
350 % 1 × 10-3 s-1
Undeformed
10 mm
Al-2024 alloy
HPT: P = 6 GPa, ω = 1 rpm, N = 5, T = R.T.
673 K
400 % 2 × 10-2 s-1
740 % 1 × 10-2 s-1
410 % 5 × 10-3 s-1
510 % 2 × 10-3 s-1
290 % 1 × 10-3 s-1
Undeformed
10 mm
Al-2024 alloy
HPT: P = 6 GPa, ω = 1 rpm, N = 5, T = R.T.
623 K
410 % 2 × 10-2 s-1
710 % 1 × 10-2 s-1
470 % 5 × 10-3 s-1
640 % 2 × 10-3 s-1
650 % 1 × 10-3 s-1
Undeformed
10 mm
Al-2024 alloy
HPT: P = 6 GPa, ω = 1 rpm, N = 5, T = R.T.
723 K
220 % 2 × 10-2 s-1
370 % 1 × 10-2 s-1
170 % 5 × 10-3 s-1
380 % 2 × 10-3 s-1
430 % 1 × 10-3 s-1
Undeformed
10 mm

Figure 9

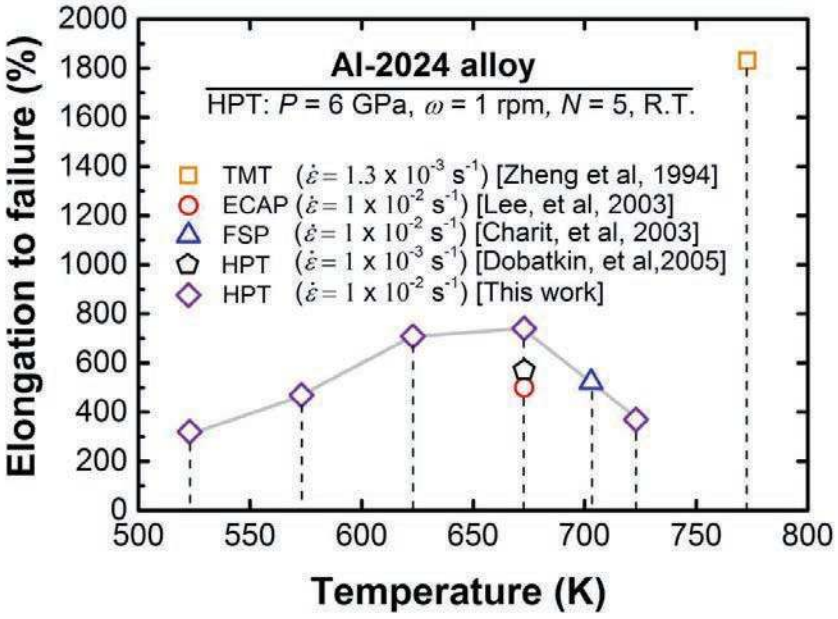
Al-2024 alloy
HPT: P = 6 GPa, ω = 1 rpm, N = 5, R.T.
TMT ($\dot{\varepsilon}$ = 1.3 x 10^{-3} s^{-1}) [Zheng et al, 1994]
ECAP ($\dot{\varepsilon}$ = 1 x 10^{-2} s^{-1}) [Lee, et al, 2003]
FSP ($\dot{\varepsilon}$ = 1 x 10^{-2} s^{-1}) [Charit, et al, 2003]
HPT ($\dot{\varepsilon}$ = 1 x 10^{-3} s^{-1}) [Dobatkin, et al,2005]
HPT ($\dot{\varepsilon}$ = 1 x 10^{-2} s^{-1}) [This work]
Elongation to failure (%)
Temperature (K)
0
200
400
600
800
1000
1200
1400
1600
1800
2000
500
550
600
650
700
750
800

Figure 10

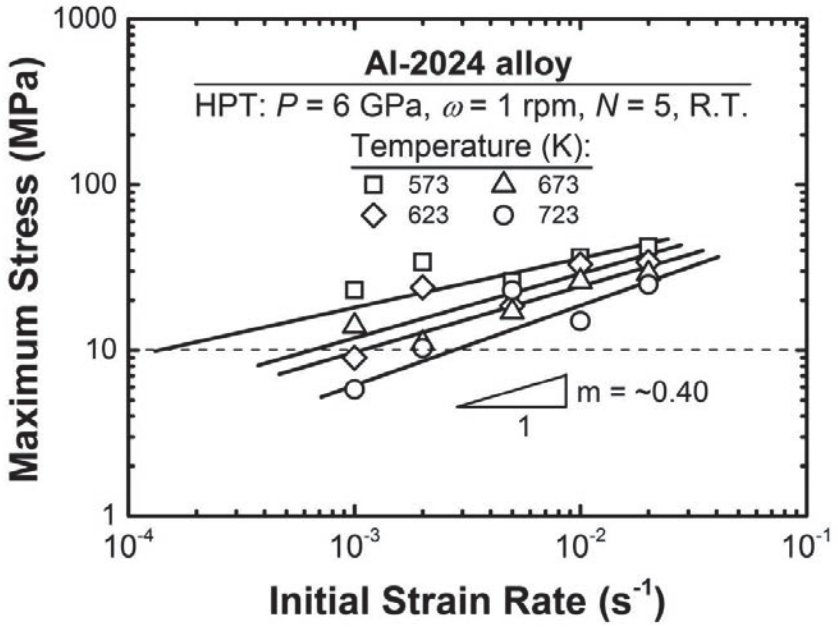
Al-2024 alloy
HPT: P = 6 GPa, ω = 1 rpm, N = 5, R.T.
Temperature (K):
573
623
673
723
m = ~0.40
1
Maximum Stress (MPa)
Initial Strain Rate (s-1)
1000
100
10
1
10-4
10-3
10-2
10-1

Figure 11

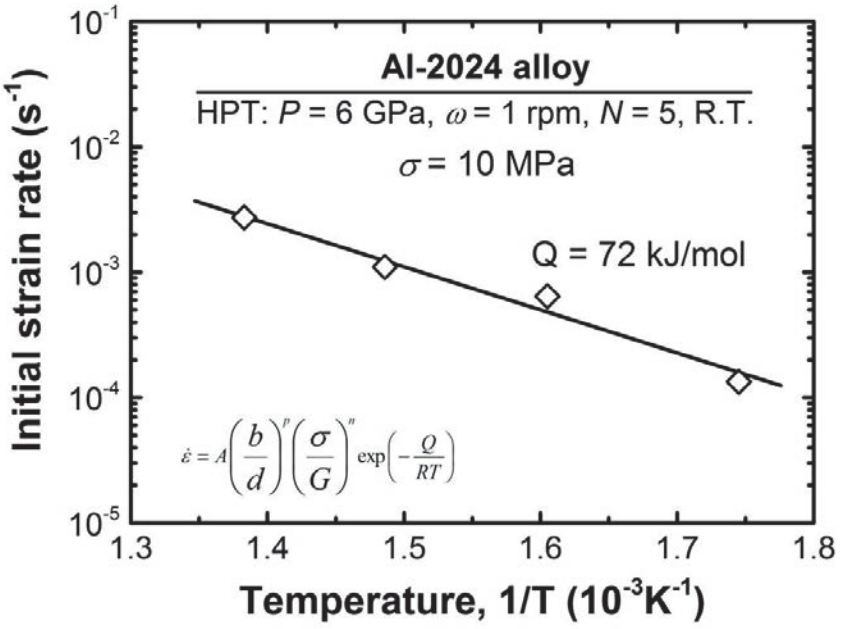
Al-2024 alloy
HPT: P = 6 GPa, ω = 1 rpm, N = 5, R.T.
σ = 10 MPa
Q = 72 kJ/mol
$\dot{\varepsilon} = A\left(\frac{b}{d}\right)^{p}\left(\frac{\sigma}{G}\right)^{n}\exp\left(-\frac{Q}{RT}\right)$
Initial strain rate (s^{-1})
Temperature, 1/T (10^{-3}K^{-1})
10^{-1}
10^{-2}
10^{-3}
10^{-4}
10^{-5}
1.3
1.4
1.5
1.6
1.7
1.8

Figure 12

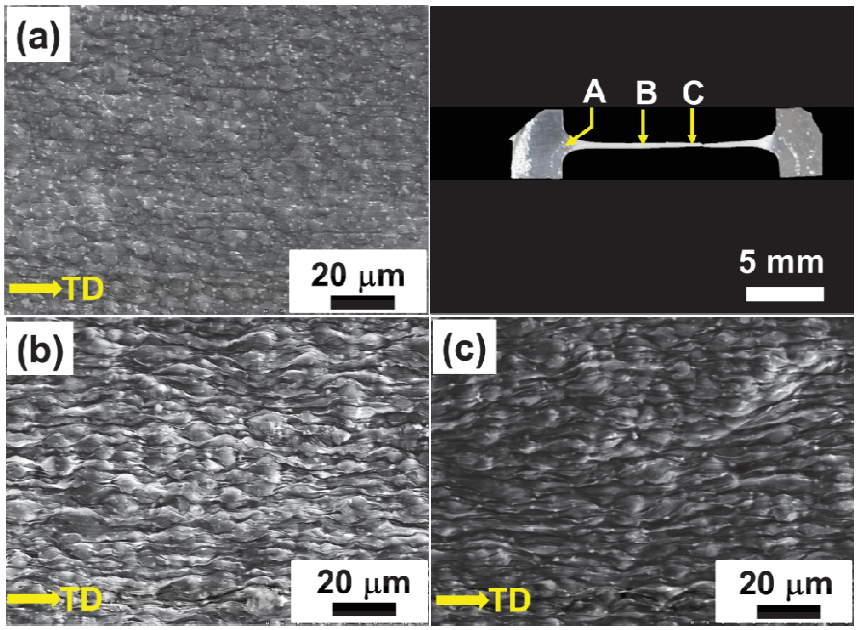

Figure 13